

ASYMPTOTIC REDUCTION OF A POROUS ELECTRODE MODEL FOR LITHIUM-ION BATTERIES*

IAIN R. MOYLES[†], MATTHEW G. HENNESSY[‡], TIMOTHY G. MYERS[§], AND
BRIAN R. WETTON[¶]

Abstract. We present a porous electrode model for lithium-ion batteries using Butler–Volmer reaction kinetics. We model lithium concentration in both the solid and fluid phase, along with solid and liquid electric potential. Through asymptotic reduction, we show that the electric potentials are spatially homogeneous, which decouples the problem into a series of time-dependent problems. These problems can be solved on three distinguished time scales: an early time scale where capacitance effects in the electrode dominate, a mid-range time scale where a spatial concentration gradient forms in the electrolyte, and a long-time scale where each of the electrodes saturate and deplete with lithium, respectively. The solid-phase concentration profiles are linear functions of time and the electrolyte potential is everywhere zero, which allows the model to be reduced to a system of two uncoupled ordinary differential equations. Analytic and numerical results are compared with full numerical simulations and experimental discharge curves, demonstrating excellent agreement.

Key words. lithium-ion battery, porous electrode model, Butler–Volmer kinetics, electrochemistry, mathematical modelling, asymptotic analysis, volume averaging, model reduction

AMS subject classifications. 78A57, 34E10, 34K26

DOI. 10.1137/18M1189579

1. Introduction. Rechargeable lithium-ion batteries (LIBs) are ubiquitous in society, utilized in medical devices, mobile phones, and transportation vehicles such as cars and airplanes. LIBs currently dominate the energy storage market compared to other batteries mostly due to a long lifespan, high energy densities, and low self-discharge rates [50]. As society moves to lessen the demands on traditional energy sources and increase the demands of portable electronics, higher capacity and safer LIBs are required.

Experimental studies are crucial in improving battery performance and lifespan [25, 26, 49]. However, battery prototypes are expensive to produce since a large number of experiments are required to assess the impact of new designs. Mathematical modelling can alleviate this pressure by providing a means to identify, simulate, and simplify dominant physics in battery operation at a fraction of the cost.

*Received by the editors May 24, 2018; accepted for publication (in revised form) May 24, 2019; published electronically August 21, 2019.

<https://doi.org/10.1137/18M1189579>

Funding: This work was supported by an Irish Research Council New Foundations grant. The work of the first author was supported by the Science Foundation Ireland under grant SFI/13/IA/1923. The work of the second author was supported by a travel grant from the Mathematics and Applications Consortium for Science and Industry from the University of Limerick. The work of the third author was supported by Ministerio de Ciencia e Innovación grant MTM2017-82317-P. The work of the second and third authors was also partially supported by the CERCA Programme of the Generalitat de Catalunya and the European Union’s Horizon 2020 research and innovation programme under Marie Skłodowska-Curie grant agreement 707658.

[†]Department of Mathematics and Statistics, York University, 4700 Keele Street, Toronto, Ontario, M3J 1P3, Canada (imoyles@yorku.ca).

[‡]Mathematical Institute, University of Oxford, Andrew Wiles Building, Radcliffe Observatory Quater, Woodstock Road, Oxford, OX2 6GG, United Kingdom (hennessy@maths.ox.ac.uk).

[§]Centre de Recerca Matemàtica, 08193 Bellaterra, Barcelona, Spain (tmyers@crm.cat).

[¶]Department of Mathematics, University of British Columbia, Vancouver, British Columbia, V6T 1Z2, Canada (wetton@math.ubc.ca).

Since the seminal work of Newman [34], who pioneered continuum modelling of porous electrochemical batteries, a plethora of works have appeared that address mathematical models and their simulation to varying degrees of complexity. A full review of these results is beyond the scope of this manuscript; however, recent overviews can be found in [19, 38]. Generally, theoretical developments follow three categories: (i) improved physical and electrochemical modelling [10, 11, 13, 18, 22, 23, 33, 35, 37, 46, 47, 5, 6, 21, 31, 45], (ii) analysis of mathematical models [40, 41], and (iii) large-scale model simulation [2, 3, 28, 43].

Articles associated with (i) focus on modelling new electrochemical and physical processes or improving current models. This involves modelling capacitance processes [35, 5, 6, 21, 31], intercalation kinetics [47, 45], active-material utilization [10], mechanics [7, 16], phase separation [46, 14, 15, 36], and applying modelling results to commercial batteries. While these models often advance the understanding of battery physics, they can be cumbersome to solve and may not elucidate dominant processes during battery operation. Articles under (ii) which address model analysis have considered the asymptotic reduction of homogenized battery models in the limit of small lithium concentration in the open-circuit potential [40] and also derived appropriate Butler–Volmer boundary conditions using matched asymptotic expansions [41]. This approach attempts to identify the equations in a model which are most responsible for an observed behavior, but sometimes requires unrealistic parameter values or leads to conclusions which cannot be related to practical batteries. Large-scale simulations in (iii) tend to focus on adding complexities to simple models and studying the results. These include using concentrated solution theory for the electrolyte, including temperature and compositional dependence in model parameters, and introducing different modelling domains for the solid and liquid phases. This approach tends to better address battery practicality since realistic battery parameters and geometries can be utilized. Large-scale simulations tend to be computationally expensive and are implemented in commercial software; however, optimized algorithms built on state-of-the-art routines can reduce some of the computational challenges.

The aim of this paper is to bridge the areas of modelling, analysis, and simulation by performing a systematic asymptotic reduction of a practical model of LIBs. The model is similar to that derived by Newman and co-authors [32, 33] that uses porous electrode theory and that utilized by An et al. [3], Li et al. [28], and Amiribavandpour et al. [2] to study the behavior of commercial LIBs. The simulation results of the latter two papers indicate that concentration profiles quickly settle into a steady state or evolve linearly with time, and we will systematically show how this occurs. We compare ours to experimental results of Li et al. and show excellent agreement.

The paper is organized as follows. We summarize the nondimensional volume-averaged porous electrode model in section 2. We state an asymptotically reduced LIB model in section 3 and derive it by exploiting the smallness of dimensionless parameters. We show how the asymptotic analysis admits analytical solutions valid over a series of time regimes which describe the entire battery discharge process. The asymptotic solutions are compared against numerical simulations in section 4 and battery discharge data in subsection 4.1. A discussion of the results follows in section 5 and the paper concludes in section 6.

2. Model overview. We consider the electrochemical processes that occur in a single cell of an LIB, as shown in Figure 1. The cell is composed of a positive (P) electrode, a separator (S), and a negative (N) electrode. The cell is assumed to be two dimensional with length L and height H . The horizontal and vertical coordinates

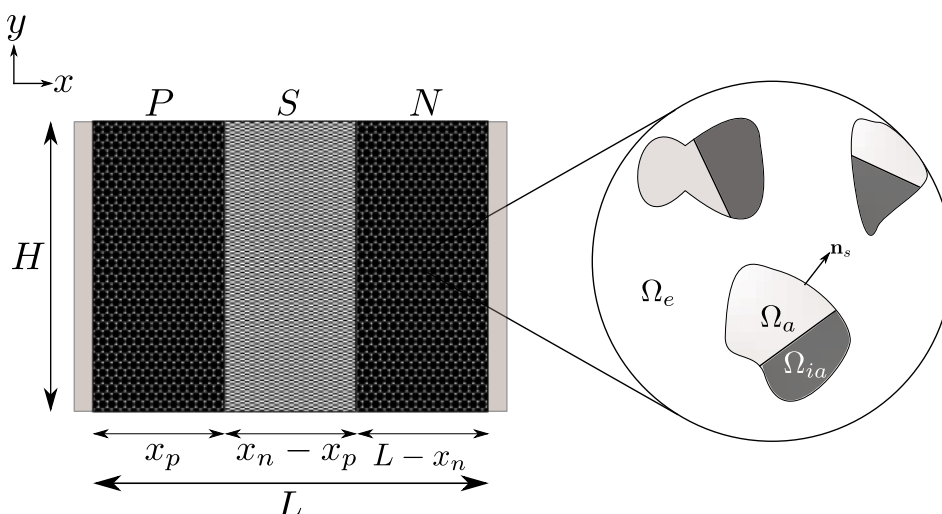


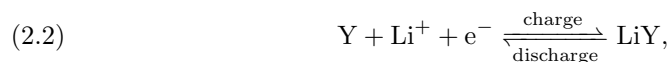
FIG. 1. Setup of a battery cell including the porous structure of the electrode layers.

x and y are used to describe material points within the cell. The positive electrode exists on $0 \leq x \leq x_p$, the separator on $x_p \leq x \leq x_n$, and the negative electrode on $x_n \leq x \leq L$.

The electrodes are porous and filled with an electrolyte that is able to carry ionic charge but not electrons. The solid material of each electrode contains active and inactive components. The active material carries electrons and hosts intercalated lithium which releases as ions into the electrolytic phase. A typical electrode volume element can be decomposed into three subdomains corresponding to the active (Ω_a) and inactive (Ω_{ia}) materials and the void space occupied by the electrolyte (Ω_e); see Figure 1. The positive electrode lithiates on discharge, and for this reason we assume it undergoes a chemical reaction of the form



where X is a binding agent such as CoO_2 , Mn_2O_4 , FePO_4 , and NiO_2 [53]. Similarly, for the negative electrode, which delithiates on discharge, we assume a reaction of the form



where a typical binding agent Y is graphite (C_6) [53]. The electrolyte is composed of a lithium salt in solvent and dissociates according to



where typical examples of the anion A are PF_6 , AsF_6 , ClO_4 , and BF_4 [53].

The separator is a perforated micro-plastic so as to be electrically insulated yet allow for the flow of ions between the electrodes. This separator is necessary to prevent the two electrodes from touching and causing a short circuit, which would negatively impact battery performance and potentially cause safety issues such as an explosion, of which many incidents have been reported [1]. A separator volume element can be

decomposed into two subdomains corresponding to inactive solid material (Ω_{ia}) and void space filled with electrolyte (Ω_{e}).

Following the pioneering work of Newman and co-authors [23, 32, 33, 34], we will model the solid and liquid phases in the three cell components using equations for conservation of mass and charge and techniques from volume averaging [4, 5, 17, 24, 54]. Volume averaging is also used in models of deionization processes where current is applied to porous electrodes in aqueous solutions [5, 6, 31].

The volume-average approach to modelling lithium transport in the solid phase of the electrode can be related to the pseudo-two-dimensional (P2D) approach developed by Doyle, Fuller, and Newman [11]. In the P2D model, the solid matrix of the electrode is envisioned as a collection of spherical particles. Accounting for solid-phase lithium transport amounts to solving the radial diffusion equation at specific points in the macroscale domain. Volume averaging the P2D geometry leads to the model that we will consider and simplifies the problem geometry at the expense of losing information about the particle surface concentration. If diffusion of lithium in the particles is fast, then the bulk and surface concentrations will be roughly equal, and the volume-averaged concentration will be an accurate representation of the microscale composition. One exception to this argument is the case of phase-separating electrodes, which undergo a mosaic instability whereby (de)lithiation occurs in isolated groups of particles in the electrode [29] rather than homogeneously across the electrode. Although resolving such features requires a P2D-style model that explicitly accounts for the microscale, volume-averaged models have been shown to produce remarkably similar predictions of macroscopic quantities such as cell potential [36]. The reason for this will be explained below.

To facilitate the asymptotic analysis and the identification of the primary electrochemical processes that occur during battery operation, we make the following modelling assumptions:

- The lithium-ion cell is one dimensional.
- The temperature remains constant.
- The material properties are independent of composition.
- Dilute solution theory is used to describe the electrolyte.
- Phase separation in the electrodes is not explicitly considered.
- The electrostatic double layer that forms at the matrix-pore interface follows the Helmholtz model.

One-dimensional geometry is motivated by the small aspect ratio ($L/H \simeq 10^{-3}$) of a typical battery cell [28, 43]. Although heat generation can be significant [55], we assume there is sufficient heat exchange with the surrounding cells and the environment to maintain a constant temperature. Valøen and Reimers [52] measured the diffusivity and ionic conductivity as a function of lithium salt concentration and showed that neither parameter changes its order of magnitude. A similar conclusion is reached from the data of Sethurajan et al. [44]. Along with these observations, the change in electrolyte composition is expected to be small (as verified below), motivating the use of dilute solution theory and constant parameters.

Phase separation occurs in many electrode materials (e.g., LiFePO_4 or LFP). In addition to triggering the mosaic instability described above, phase separation also plays a key role in controlling the open-circuit potential [14, 15]. While neglecting phase separation may seem like a severe limitation of our proposed model, it is possible to partially account for the electrochemical impact of this process through the use of an appropriate chemical potential [36, 51] (or, equivalently, an open-circuit potential) in the reaction kinetics. In subsection 4.1 we will show that the asymptotically reduced

model derived here can accurately predict the experimental discharge curves of an LFP cell using an empirical open-circuit potential.

When the charged solid matrix contacts a liquid electrolyte, an electrostatic double layer forms as co- and countercharges are repelled and attracted, respectively. This layer typically has two parts: a Stern layer where counterions adhere to the matrix surface, creating a molecular dielectric with a fixed capacitance, and a diffuse layer where charges are free to move, diminishing the electrostatic effects of the charged matrix with distance. The Helmholtz model assumes that the Stern layer is much thicker than the diffuse layer, ignoring the latter's effect on the potential difference between the solid and electrolyte. This assumption is frequently used in lithium-ion battery modelling [28, 43, 42, 46], although inclusion of diffuse-layer effects has been considerably discussed in models of deionization [6, 21, 45]. The main impact of choosing how to model the electrostatic double layer is seen in the form of reaction kinetics as we will discuss in subsection 2.2.

2.1. Bulk equations. The roman subscript $i = n, p, s$ is used to denote the negative electrode, positive electrode, and separator, respectively. The notation $\psi_{j,i}$ therefore represents the quantity ψ_j in component i . Due to the abundance of literature based on porous electrode theory, we will present our model in nondimensional form. However, a description of the full-dimensional equations and their derivation appears in supplemental section SM1 for posterity.

In nondimensionalizing, space is scaled with the length L of the cell, time with the diffusive time scale of lithium in the electrolyte L^2/D_L , and current densities with the nominal applied current density i_0 . Concentrations and electric potentials (including open-circuit potentials) are written as the deviation from their initial values and scaled with the change due to electrochemical reactions $(i_0 L)/(FD_L)$ and the thermal voltage RT_a/F , respectively, where R is the universal gas constant, F is Faraday's constant, and T_a is the ambient temperature.

Volume averaging for conservation of mass and charge of the active solid phase in electrode i results in

$$(2.4a) \quad \frac{\partial c_{a,i}}{\partial t} = \mathcal{D}_i \frac{\partial^2 c_{a,i}}{\partial x^2} + \frac{\partial i_{a,i}}{\partial x},$$

$$(2.4b) \quad \nu_{a,i} i_{a,i} = -\frac{\partial \Phi_{a,i}}{\partial x},$$

$$(2.4c) \quad \phi_{a,i} \frac{\partial i_{a,i}}{\partial x} = -\mathcal{G}_i \left(g_i + \mathcal{C}_i \frac{\partial}{\partial t} (\Phi_{a,i} - \Phi_{e,i}) \right),$$

where t is time, x is the horizontal coordinate, $c_{a,i}$ is the concentration of intercalated lithium, $i_{a,i}$ is the current density in the active solid phase, and $\Phi_{a,i}$ and $\Phi_{e,i}$ are the electric potential in the active solid and electrolyte, respectively. The concentration $c_{a,i}$ can be interpreted as that which arises from volume averaging over several particles in the P2D model. The parameter \mathcal{D}_i is the ratio of solid-phase to liquid-phase lithium diffusivity. The quantity g_i is the nondimensional surface-averaged electrochemical current that is produced at the electrode-electrolyte interface, which will be defined in subsection 2.2. Associated with it is the parameter \mathcal{G}_i which is the ratio of current produced by surface reactions to the input current of the system. The parameter $\phi_{a,i}$ is the volume fraction of active solid material, \mathcal{C}_i is the nondimensional capacitance associated with a double-charging layer, and $\nu_{a,i}$ is a nondimensional resistivity.

Similar equations follow for the fluid phase by averaging over the electrolyte vol-

ume:

$$(2.5a) \quad \frac{\partial c_{L,i}}{\partial t} = \frac{\partial}{\partial x} \left(\frac{\partial c_{L,i}}{\partial x} + \nu_e^{-1} \theta (1 + \gamma c_{L,i}) \frac{\partial \Phi_{e,i}}{\partial x} \right) + \frac{\partial i_{e,i}}{\partial x},$$

$$(2.5b) \quad i_{e,i} = -(1 - \mathcal{D}_A) \frac{\partial c_{L,i}}{\partial x} - \nu_e^{-1} (1 + \gamma c_{L,i}) \frac{\partial \Phi_{e,i}}{\partial x},$$

$$(2.5c) \quad \phi_{e,i} \frac{\partial i_{e,i}}{\partial x} = \mathcal{G}_i \left(g_i + \mathcal{C}_i \frac{\partial}{\partial t} (\Phi_{a,i} - \Phi_{e,i}) \right).$$

Here, $c_{L,i}$ is the concentration of lithium ions in the electrolyte, $i_{e,i}$ is the electrolytic current, and $\phi_{e,i}$ is the volume fraction of the electrolyte. We do not explicitly model the concentration of anions because electroneutrality requires that it be the same as the lithium concentration. The parameter \mathcal{D}_A is the ratio of anion diffusivity to lithium-ion diffusivity in the electrolyte, θ is the transference number, ν_e is a nondimensional electrolyte resistivity, and γ is the relative change in lithium ion concentration from its initial value. A phase-averaged conservation of charge emerges by adding (2.4c) and (2.5c),

$$(2.6) \quad \frac{\partial}{\partial x} (\phi_{a,i} i_{a,i} + \phi_{e,i} i_{e,i}) = 0,$$

which will be used in place of (2.5c).

Finally, the nondimensional model in the separator is

$$(2.7a) \quad \frac{\partial c_{L,s}}{\partial t} = \frac{\partial}{\partial x} \left(\frac{\partial c_{L,s}}{\partial x} + \nu_e^{-1} \theta (1 + \gamma c_{L,s}) \frac{\partial \Phi_{e,s}}{\partial x} \right),$$

$$(2.7b) \quad i_{e,s} = -(1 - \mathcal{D}_A) \frac{\partial c_{L,s}}{\partial x} - \nu_e^{-1} (1 + \gamma c_{L,s}) \frac{\partial \Phi_{e,s}}{\partial x},$$

$$(2.7c) \quad \frac{\partial i_{e,s}}{\partial x} = 0,$$

where the main change to the electrolyte problem in the electrode is the absence of surface reaction currents. We can eliminate the electrolyte potential from the liquid equations in the electrode (by manipulating (2.5a) and (2.5b)) and separator (by manipulating (2.7a) and (2.7b)), resulting in

$$(2.8a) \quad \frac{\partial c_{L,i}}{\partial t} = \mathcal{R} \frac{\partial^2 c_{L,i}}{\partial x^2} + (1 - \theta) \frac{\partial i_{e,i}}{\partial x},$$

$$(2.8b) \quad \frac{\partial c_{L,s}}{\partial t} = \mathcal{R} \frac{\partial^2 c_{L,s}}{\partial x^2},$$

where $\mathcal{R} = 1 - \theta(1 - \mathcal{D}_A)$.

The cell voltage, ΔV , is determined as the difference in the potentials in the solid phase of the positive electrode at $x = 0$ and negative electrode at $x = L$,

$$(2.9) \quad \Delta V = \Phi_{a,p}(0, t) - \Phi_{a,n}(L, t) + \log \mathcal{U}_p - \log \mathcal{U}_n,$$

where $(RT_a/F) \log \mathcal{U}_i$ represents the initial value of the dimensional open-circuit potential. An expression for \mathcal{U}_i in terms of reaction constants is given in (SM1.49) in the supplementary material.

2.2. Reaction kinetics. The surface reaction currents g_i are described by the Butler–Volmer kinetics [11, 18, 32, 33] in the Helmholtz limit valid for thin electric double layers at high salt concentrations [46]. This means that we will neglect the Frumkin correction which explicitly creates a dependence of the reaction rate on the local electric field near the surface of the solid matrix (see supplementary subsection SM1.5 for more details). The Helmholtz assumption could limit practically achievable power densities at high discharge rates when the electrolyte salt becomes depleted [46].

Along with the Helmholtz assumption, we prescribe a theoretical open-circuit potential following Newman [32, page 212] (see supplementary subsection SM1.5). This defines the nondimensional Butler–Volmer reaction kinetics as

$$(2.10a) \quad g_i = j_i (\exp [(1 - \beta_i)\eta_i] - \exp [-\beta_i\eta_i]),$$

$$(2.10b) \quad j_i = (1 + \delta_i \gamma c_{a,i})^{\beta_i} (1 - \delta_i \xi_i (1 - \xi_i)^{-1} \gamma c_{a,i})^{1-\beta_i} (1 + \gamma c_{L,i})^{1-\beta_i}.$$

The surface overpotential is defined by $\eta_i = \Phi_{a,i} - \Phi_{e,i} - U_i$, with

$$(2.11) \quad U_i = \log \mathcal{V}_i, \quad \mathcal{V}_i = \frac{(1 + \gamma c_{L,i})[1 - \delta_i \xi_i (1 - \xi_i)^{-1} \gamma c_{a,i}]}{1 + \delta_i \gamma c_{a,i}},$$

denoting the open-circuit potential. The parameter β_i is a symmetry factor, δ_i is the ratio of initial lithium in the electrolyte to solid, and ξ_i is the ratio of the initial solid concentration to the maximum amount allowed in the electrode. This is also the initial state of charge. By extending the form of the open-circuit potential (2.11), it is possible to account for additional physics such as phase separation [14, 15, 36] and multiple lithiation stages [15, 51] in the volume-averaged model.

2.3. Boundary and initial conditions. The electrolyte is free to flow between the voids of the electrodes and separator. Therefore, we require the concentration and molar flux of lithium ions and the current density in the electrolyte, as well as the electrolyte potential, to be continuous. Continuity of flux and current can be simplified to yield continuity in the derivatives of lithium concentration and electrolyte potential:

$$(2.12a) \quad c_{L,i} - c_{L,s} = 0, \quad x = x_p, x_n,$$

$$(2.12b) \quad \phi_{e,i} \frac{\partial c_{L,i}}{\partial x} - \phi_{e,s} \frac{\partial c_{L,s}}{\partial x} = 0, \quad x = x_p, x_n,$$

$$(2.12c) \quad \phi_{e,i} \frac{\partial \Phi_{e,i}}{\partial x} - \phi_{e,s} \frac{\partial \Phi_{e,s}}{\partial x} = 0, \quad x = x_p, x_n,$$

$$(2.12d) \quad \Phi_{e,i} - \Phi_{e,s} = 0, \quad x = x_p, x_n.$$

The volume fractions appearing in (2.12) account for differences in the porosity of each material and arise from the process of averaging the microscopic boundary conditions. The solid component of the separator is electrically inactive and, therefore, no current can pass through it:

$$(2.13) \quad i_{a,i} = 0, \quad x = x_p, x_n.$$

The electrode surfaces at $x = 0$ and $x = 1$ are in contact with current collectors which enable electric charge to be injected into and extracted from the cell during charging and discharging. We focus on the case of battery discharging and, therefore, assume that a nondimensional current density of \mathcal{I} is being drawn from the positive

electrode. This value is also known as the C-rate of the battery, where $\mathcal{I} = 1$ is equivalent to the battery fully discharging over an hour at its nominal rate (see supplementary subsection SM1.3 for more details). The discharge boundary condition is

$$(2.14) \quad \phi_{a,p} i_{a,p} = -\mathcal{I}, \quad x = 0,$$

where the negative sign on the right-hand side indicates a discharge process.

Without loss of generality, we can set the electrolyte potential in the negative electrode to zero at the electrode-collector interface, leading to

$$(2.15) \quad \Phi_{e,n} = 0, \quad x = 1.$$

The current collectors are impermeable and, therefore, the molar fluxes, and hence the current, of the electrolyte must vanish at the electrode-collector interfaces,

$$(2.16) \quad i_{e,i} = 0, \quad x = 0, 1.$$

Similar to the electrode-separator interfaces, we can combine the vanishing molar flux condition for both lithium and anionic species, which produces a Neumann condition for the lithium concentration,

$$(2.17) \quad \frac{\partial c_{L,i}}{\partial x} = 0, \quad x = 0, 1.$$

The mass flux of the solid lithium must also vanish at the electrode boundaries:

$$(2.18) \quad \frac{\partial c_{a,i}}{\partial x} = 0, \quad x = 0, x_p, x_n, 1.$$

The initial conditions are given by $c_{a,i}(x, 0) = 0$, $c_{L,i}(x, 0) = 0$, $\Phi_{e,i}(x, 0) = 0$, and $\Phi_{a,i}(x, 0) = 0$ because of the choice of nondimensionalisation.

3. Asymptotic reduction. The main result of this paper is to systematically derive a reduced model for an LIB of the form

$$(3.1a) \quad \mathcal{C}_n \frac{d\Phi_{a,n}}{dt} = \frac{\mathcal{I}}{\mathcal{G}_n(1-x_n)} - g_n(\Phi_{a,n}, c_{a,n}), \quad c_{a,n} = -\frac{\mathcal{I}}{\phi_{a,n}(1-x_n)}t,$$

$$(3.1b) \quad \mathcal{C}_p \frac{d\Phi_{a,p}}{dt} = -\frac{\mathcal{I}}{\mathcal{G}_p x_p} - g_p(\Phi_{a,p}, c_{a,p}), \quad c_{a,p} = -\frac{\mathcal{I}}{\phi_{a,p} x_p}t,$$

with $\Phi_{a,i}(0) = 0$. To obtain (3.1), we carry out a preliminary reduction of the full nondimensional model using regular perturbation theory, followed by a detailed asymptotic analysis using singular perturbation theory. This is now discussed in detail.

3.1. Preliminary model reduction. Physical constants for different batteries are presented throughout the literature [2, 28, 35, 40] and generally result in all of the parameters in (2.4), (2.5), and (2.7) being small except for \mathcal{D}_A , \mathcal{G}_i , ξ_i , δ_i , and \mathcal{U}_i . The order one assumptions for δ_i and ξ_i are generally only true for the initially lithiated electrode.

Using the parameter sizes considered above, the model is naturally reduced by neglecting all parameters which are less than $\mathcal{O}(1)$ in size. We can set $\mathcal{D}_i \rightarrow 0$ in (2.4a), as the no-flux conditions for $c_{a,i}$ given by (2.18) are consistent with the spatially uniform initial condition so boundary layers are avoided. Taking $\nu_e \rightarrow 0$ in (2.5b) and

(2.7b) shows that the electrolyte potential $\Phi_{e,i}$ is constant in space, and through the continuity and grounding conditions (2.12d) and (2.15) must be zero everywhere, $\Phi_{e,i} \equiv 0$. Similarly, taking $\nu_{a,i} \rightarrow 0$ in (2.4b) shows that the active solid potential is constant in space. Finally, although \mathcal{C}_i and γ are small, setting them to zero leads to singular limits representing distinguished time regimes which we study using matched asymptotic expansions. The singular limit for \mathcal{C}_i arises because it is multiplying a time derivative of the potential marking an early time regime where capacitance effects are relevant. The singular limit for γ is less obvious but arises from the reaction currents in (2.10b) and \mathcal{V}_i in (2.11), which suggest the possibility of a regime where the concentrations are $\mathcal{O}(\gamma^{-1})$ in size, corresponding to the depletion/saturation of lithium in the electrodes.

Taking the limit as $\mathcal{D}_i \rightarrow 0$, $\nu_e \rightarrow 0$, and $\nu_{a,i} \rightarrow 0$, while retaining the parameters \mathcal{C}_i and γ , leads to a simplified set of bulk equations given by

$$(3.2a) \quad \frac{\partial c_{a,i}}{\partial t} = \frac{\partial i_{a,i}}{\partial x},$$

$$(3.2b) \quad \phi_{a,i} \frac{\partial i_{a,i}}{\partial x} = -\mathcal{G}_i \left(g_i + \mathcal{C}_i \frac{d\Phi_{a,i}}{dt} \right),$$

$$(3.2c) \quad \frac{\partial c_{L,i}}{\partial t} = \mathcal{R} \frac{\partial^2 c_{L,i}}{\partial x^2} + (1 - \theta) \frac{\partial i_{e,i}}{\partial x}$$

for the electrodes and

$$(3.3) \quad \frac{\partial c_{L,s}}{\partial t} = \mathcal{R} \frac{\partial^2 c_{L,s}}{\partial x^2}$$

for the separator. Governing equations for the electrolyte current are not required as the one-dimensional charge conservation condition (2.6) can be integrated to find that

$$(3.4) \quad \phi_{a,i} i_{a,i} + \phi_{e,i} i_{e,i} = -\mathcal{I}$$

in each of the cell components, where the boundary conditions (2.13), (2.14), and (2.16) have been used. The Butler–Volmer kinetics are given by (2.10) and (2.11) with a reduced overpotential $\eta_i = \Phi_{a,i} - \log(\mathcal{V}_i)$.

The boundary conditions for this simplified model are given by

$$(3.5a) \quad \phi_{a,p} i_{a,p} = -\mathcal{I}, \quad x = 0,$$

$$(3.5b) \quad c_{L,i} - c_{L,s} = 0, \quad x = x_p, x_n,$$

$$(3.5c) \quad \phi_{e,i} \frac{\partial c_{L,i}}{\partial x} - \phi_{e,s} \frac{\partial c_{L,s}}{\partial x} = 0, \quad x = x_p, x_n,$$

$$(3.5d) \quad i_{a,i} = 0, \quad x = x_p, x_n,$$

$$(3.5e) \quad \frac{\partial c_{L,i}}{\partial x} = 0, \quad x = 0, 1,$$

while the initial conditions are $c_{a,i} = c_{L,i} = \Phi_{a,i} = 0$.

We now proceed to solve the simplified model using asymptotic methods. Our approach exploits the fact that, based on singular limits for \mathcal{C}_i and γ , there are three key regimes that occur during battery discharge. First, there is a small-time regime, given by $t = \mathcal{O}(\mathcal{C}_i)$, that captures the rapid formation of double charging layers at the electrode-electrolyte interfaces due to the instantaneous application of current to the

cell. In the first regime, capacitance effects play a key role and composition changes are negligible. In the second time regime, defined by $t = \mathcal{O}(1)$, capacitance effects become negligible. Electrochemical reactions lead to $\mathcal{O}(1)$ changes in the concentration of intercalated lithium ions in the electrodes and diffusive transport begins in the electrolyte. In the third and final regime, given by $t = \mathcal{O}(\gamma^{-1})$, the electrodes become fully saturated and depleted of lithium, corresponding to a drained battery. The first two regimes have previously been identified in models of desalination, with the first regime where charge storage occurs termed the supercapacitive regime while the second is the capacitive dionization regime where salt is removed [5, 6].

3.2. First regime: Double charging layer. The first regime is captured by choosing a time scale that balances both terms on the right-hand side of (3.2b). Typically [28, 43], the material properties are such that $\mathcal{C}_n \ll \mathcal{C}_p$, leading to two subregimes that must be considered. Thus, we first calculate solutions for $t = \mathcal{O}(\mathcal{C}_n)$ and then focus on the case when $t = \mathcal{O}(\mathcal{C}_p)$.

In the first subregime, we let $t = \mathcal{C}_n \tilde{t}$ in (3.2) and (3.3). Upon taking $\mathcal{C}_n \rightarrow 0$ and $\gamma \rightarrow 0$ with $c_{a,i} = \mathcal{O}(1)$ and $c_{L,i} = \mathcal{O}(1)$, we obtain

$$(3.6) \quad \frac{\partial c_{L,i}}{\partial \tilde{t}} = \frac{\partial c_{a,i}}{\partial \tilde{t}} = \frac{d\Phi_{a,p}}{d\tilde{t}} = 0.$$

Thus, the concentrations remain unchanged from their initial value: $c_{L,i} \equiv 0$ and $c_{a,i} \equiv 0$. The solid potential in the positive electrode is $\Phi_{a,p} \equiv 0$. For the negative electrode, we find

$$(3.7) \quad \phi_{a,n} \frac{\partial i_{a,n}}{\partial x} = -\mathcal{G}_n \left(g_n + \frac{d\Phi_{a,n}}{d\tilde{t}} \right).$$

Since the solid- and liquid-phase concentrations of lithium remain at zero, then $\mathcal{V}_i = 1$ and $\eta_i = \Phi_{a,i}$. Therefore, g_n is now solely a function of time and so (3.7) can be integrated in space using (3.5a) and (3.5d) to yield a differential equation for $\Phi_{a,n}$, given by

$$(3.8) \quad \frac{d\Phi_{a,n}}{d\tilde{t}} = \frac{\mathcal{I}}{\mathcal{G}_n(1-x_n)} - [\exp((1-\beta_n)\Phi_{a,n}) - \exp(-\beta_n\Phi_{a,n})],$$

where $\Phi_{a,n}(0) = 0$. Using the initial condition, we see that $d\Phi_{a,n}/d\tilde{t} > 0$ when $\tilde{t} = 0$. Thus, the potential in the negative electrode will increase in time until it reaches a steady state $\Phi_{a,n}^*$ given by

$$(3.9) \quad \exp((1-\beta_n)\Phi_{a,n}^*) - \exp(-\beta_n\Phi_{a,n}^*) = \frac{\mathcal{I}}{\mathcal{G}_n(1-x_n)}.$$

When $\beta_n = 1/2$, which is often considered in other models and corresponds to symmetric anodic and cathodic reactions, an implicit solution to (3.8) can be obtained (see supplementary section SM2). Using (2.9), the cell potential in this subregime, ΔV_I^n , is

$$(3.10) \quad \Delta V_I^n = \log \mathcal{U}_p - \Phi_{a,n} - \log \mathcal{U}_n,$$

with $\Phi_{a,n}$ computed from (3.8).

The next capacitance subregime can be analyzed by letting $t = \mathcal{C}_p \tilde{t}$ and taking $\mathcal{C}_p \rightarrow 0$ and $\gamma \rightarrow 0$ with $c_{a,i} = \mathcal{O}(1)$ and $c_{L,i} = \mathcal{O}(1)$, which still leaves the concentrations unchanged and results in the electrode kinetics

$$(3.11a) \quad 0 = \frac{\mathcal{I}}{\mathcal{G}_n(1-x_n)} - [\exp((1-\beta_n)\Phi_{a,n}) - \exp(-\beta_n\Phi_{a,n})],$$

$$(3.11b) \quad \frac{d\Phi_{a,p}}{d\tilde{t}} = -\frac{\mathcal{I}}{\mathcal{G}_p x_p} - [\exp((1-\beta_p)\Phi_{a,p}) - \exp(-\beta_p\Phi_{a,p})],$$

which have come from integrating (3.2b), as once again g_i is space independent. Equation (3.11a) prescribes a steady potential in the negative electrode phase, $\Phi_{a,n}(\tilde{t}) \equiv \Phi_{a,n}^*$, which matches that of the previous subregime. The initial condition for (3.11b) is also obtained by matching to the solution in the previous subregime, which yields $\Phi_{a,p}(0) = 0$. Equation (3.11b) describes a decreasing potential in the positive electrode to a steady state given by

$$(3.12) \quad \exp((1-\beta_p)\Phi_{a,p}^*) - \exp(-\beta_p\Phi_{a,p}^*) = -\frac{\mathcal{I}}{\mathcal{G}_p x_p}.$$

As before, analytical solutions for $\Phi_{a,p}$ and $\Phi_{a,p}^*$ can be obtained when $\beta_p = 1/2$. The cell potential in this region, ΔV_I^p , is

$$(3.13) \quad \Delta V_I^p = \Phi_{a,p} + \log \mathcal{U}_p - \Phi_{a,n}^* - \log \mathcal{U}_n,$$

where $\Phi_{a,n}^*$ is given by (3.9) and $\Phi_{a,p}$ is determined by (3.11b).

3.3. Second regime: Diffusion in liquid. We now move on to the second regime where $t = \mathcal{O}(1)$. Matching to the solutions in the first regime implies that the concentrations $c_{a,i}$ and $c_{L,i}$ must be $\mathcal{O}(1)$ in magnitude. Thus, we can take $\gamma \rightarrow 0$ to show that $\mathcal{V}_i = 1$ and g_i remains independent of space. Equation (3.2b) can be integrated as in subsection 3.2, and the limits $\mathcal{C}_i \rightarrow 0$ can be taken to obtain

$$(3.14) \quad \Phi_{a,i}(t) \equiv \Phi_{a,i}^*,$$

which automatically matches the solutions for the overpotential in the first regime. The cell voltage in this region, ΔV_{II} , is given by

$$(3.15) \quad \Delta V_{II} = \Phi_{a,p} + \log \mathcal{U}_p - \Phi_{a,n}^* - \log \mathcal{U}_n$$

and is constant in time. We also have that the active solid current densities are given by

$$(3.16) \quad i_{a,n} = -\frac{\mathcal{I}}{\phi_{a,n}(1-x_n)}(x-x_n), \quad i_{a,p} = -\frac{\mathcal{I}}{\phi_{a,p}x_p}(x_p-x),$$

which we can substitute into (3.2a) for each of the electrodes to find that the intercalated lithium-ion concentrations are

$$(3.17) \quad c_{a,n} = -\frac{\mathcal{I}}{\phi_{a,n}(1-x_n)}t, \quad c_{a,p} = \frac{\mathcal{I}}{\phi_{a,p}x_p}t,$$

where we have used the matching conditions $c_{a,i} \sim 0$ as $t \sim 0$. In principle, the concentration of lithium ions in the electrolyte, $c_{L,i}$, can be obtained using separation of variables, as has been utilized in models without intercalation kinetics [12, 20].

However, for our purposes, it is sufficient to consider the steady-state concentration profile given by

$$(3.18a) \quad c_L^* = \frac{(1-\theta)\mathcal{I}}{2\mathcal{R}\phi_e} \begin{cases} (x^2/x_p + (2\phi_e/\phi_{e,s} - 1)x_p + \mathcal{B}), & 0 \leq x \leq x_p, \\ ((2\phi_e/\phi_{e,s})x + \mathcal{B}), & x_p \leq x \leq x_n, \\ (1 + (2\phi_e/\phi_{e,s} - 1)x_n - (1-x)^2/(1-x_n) + \mathcal{B}), & x_n \leq x \leq 1, \end{cases}$$

where

$$(3.18b) \quad \mathcal{B} = \frac{\phi_e}{\phi_e x_p + \phi_{e,s}(x_n - x_p) + \phi_e(1 - x_n)} \times \left\{ \frac{1}{3} [(1 - x_n)^2 - x_p^2] + 2 \left(1 - \frac{\phi_e}{\phi_{e,s}} \right) [x_n(1 - x_n) + x_p^2] - 1 \right\}.$$

In deriving (3.18a), we have used the fact that

$$(3.19) \quad \int_0^{x_p} \phi_e c_{L,p} \, dx + \int_{x_p}^{x_n} \phi_{e,s} c_{L,s} \, dx + \int_{x_n}^1 \phi_e c_{L,n} \, dx = 0$$

for all time, which arises from the no-flux boundary conditions at the electrode-collector interfaces and continuity of flux across the electrode-separator interfaces, implying that the total concentration of lithium in the electrolyte is a conserved quantity.

3.4. Third regime: Electrode saturation/depletion. The linear growth and decay of the concentration of intercalated lithium in (3.17) necessitates a large-time regime where the finite capacity of the electrodes must be taken into consideration. Mathematically, this means capturing the composition dependence of the Butler–Volmer kinetics (2.10). In the first and second regimes, this dependence could be removed by taking the limit as $\gamma \rightarrow 0$ with $c_{a,i} = \mathcal{O}(1)$. We now account for large changes in $c_{a,i}$ which alter the details of this limit.

An examination of the expression for g_i given by (2.10) shows that the composition dependence becomes relevant when the concentrations $c_{a,i}$ become $\mathcal{O}(\gamma^{-1})$ in size. From (3.17), this concentration scale corresponds to a time scale of $t = \mathcal{O}(\gamma^{-1})$. Thus, in the third regime, we write $t = \gamma^{-1}\hat{t}$, $c_{a,i} = \gamma^{-1}\hat{c}_{a,i}$, and $\Phi = \hat{\Phi}_{a,i}$. There is no need to rescale the concentration of lithium in the electrolyte since matching to the second regime implies $c_{L,i} = \mathcal{O}(1)$. With this scaling, it is then possible to take $\mathcal{C}_i \rightarrow 0$ and $\gamma \rightarrow 0$ as before. The limit $\gamma \rightarrow 0$ removes the dependence of g_i on $c_{L,i}$; however, the dependence on $\hat{c}_{a,i}$ is retained because $\mathcal{V}_i \neq 1$. The matching conditions for $\hat{c}_{a,i}$ are given by

$$(3.20) \quad \hat{c}_{a,n} = -\frac{\mathcal{I}}{\phi_{a,n}(1 - x_n)}\hat{t}, \quad \hat{c}_{a,p} = \frac{\mathcal{I}}{\phi_{a,p}x_p}\hat{t},$$

as $\hat{t} \sim 0$, which implies that $\hat{c}_{a,i}$ and hence g_i will be independent of space for all time. The same procedure as in the first and second time regimes can then be used to obtain solutions in the third regime. The concentrations of intercalated lithium are given by (3.20), the concentration of lithium ions in the electrolyte is constant in

time and given by (3.18a), and the current densities are those in (3.16). The electrode kinetics can be written in terms of the concentrations as

$$(3.21a) \quad \begin{aligned} \frac{\mathcal{I}}{\mathcal{G}_n(1-x_n)} &= (1 + \delta_n \hat{c}_{a,n}) \exp((1 - \beta_n) \hat{\Phi}_{a,n}) \\ &\quad - (1 - \delta_n \xi_n (1 - \xi_n)^{-1} \hat{c}_{a,n}) \exp(-\beta_n \hat{\Phi}_{a,n}), \end{aligned}$$

$$(3.21b) \quad \begin{aligned} -\frac{\mathcal{I}}{\mathcal{G}_p x_p} &= (1 + \delta_p \hat{c}_{a,p}) \exp((1 - \beta_p) \hat{\Phi}_{a,p}) \\ &\quad - (1 - \delta_p \xi_p (1 - \xi_p)^{-1} \hat{c}_{a,p}) \exp(-\beta_p \hat{\Phi}_{a,p}). \end{aligned}$$

The cell voltage in this regime, ΔV_{III} , is given by

$$(3.22) \quad \Delta V_{\text{III}} = \hat{\Phi}_{a,p} + \log \mathcal{U}_p - \hat{\Phi}_{a,n} - \log \mathcal{U}_n,$$

where $\hat{\Phi}_{a,i}$ comes from solving (3.21) with the time-dependent concentrations given by (3.20).

An examination of (3.21) reveals that the electrode potential $\hat{\Phi}_{a,i}$ becomes singular at finite concentrations given by

$$(3.23a) \quad \hat{c}_{a,i} = -\frac{1}{\delta_i} \quad \text{leading to } \hat{\Phi}_{a,i} \rightarrow \infty,$$

$$(3.23b) \quad \hat{c}_{a,i} = \frac{1 - \xi_i}{\delta_i \xi_i} \quad \text{leading to } \hat{\Phi}_{a,i} \rightarrow -\infty.$$

These are precisely the nondimensional variants of the two limiting (dimensional) concentrations, $c_{a,i} = 0$ and $c_{a,i} = c_{a,i}^{\max}$, respectively.

At first appearance, it seems the physically infeasible unbounded growth and decay of the concentration of intercalated lithium has not been resolved, as the solutions (3.20) indicate that the linear dependence on time persists. However, in consideration of the limits in (3.23), finite-time blow-up occurs in the electric potential as these terminal concentrations are approached. In the negative electrode, $\hat{c}_{a,n}$ decreases so (3.23a) gives the terminal value of $\hat{c}_{a,n}$. Similarly, (3.23b) gives the limiting value for $\hat{c}_{a,p}$. Using (3.20), the terminal concentrations in (3.23) correspond to blow-up times given by

$$(3.24) \quad \hat{t}_n = \frac{\phi_{a,n}(1-x_n)}{\delta_n \mathcal{I}}, \quad \hat{t}_p = \frac{\phi_{a,p} x_p (1 - \xi_p)}{\delta_p \xi_p \mathcal{I}}.$$

Physically, the finite-time blow-up corresponds to a failure of the model where a constant discharge/charge current \mathcal{I} is no longer feasible and the battery stops operating at

$$(3.25) \quad \hat{t}_c = \min\{\hat{t}_n, \hat{t}_p\}.$$

Finite-time blow-up is rarely mentioned in other models, as simulations are typically terminated based on a threshold value of the cell potential [28].

3.5. Construction of the composite reduced model. We can now construct the composite model (3.1), and generalize it to account for general open-circuit potentials, by recognizing that regardless of the open-circuit potential, the electrolyte concentration always reaches an $\mathcal{O}(1)$ steady state, c_L^* given by (3.18a), in $\mathcal{O}(1)$ time as per the analysis of regime 2 in subsection 3.3. Consequently, we can ignore the

electrolyte concentration when solving for the electric potentials. We also have that the solid-phase concentrations $c_{a,i}$ are spatially uniform, linear functions of time given by (3.17), which are valid throughout all three regimes. Therefore, the main impact of each regime is to change the voltage dynamics, primarily from open-circuit conditions in regime 1 to saturation/depletion conditions in regime 3. For this reason we can pose the composite reduced model by retaining the two singular contributions, leading to the model given by (3.1), where g_i is the full concentration-dependent reaction kinetics defined by (2.10), but now with an arbitrary form of the open-circuit potential U_i . For consistency with the nondimensionalization, the initial value of U_i must be zero, with the initial value of the dimensional open-circuit potential being equal to $(RT_a/F)\log \mathcal{U}_i$. The composite model (3.1) has both the powerful simplicity of the asymptotic reduction and the versatility to easily handle a variety of open-circuit potentials U_i that extend those given by (2.11).

4. Comparison with numerics. We now compare the asymptotic reduction from section 3 to simulations of the full model to assess the accuracy of our approach. We take $\mathcal{D}_A = \mathcal{G}_n = \mathcal{G}_p = \mathcal{I} = \mathcal{R} = 1$, as these have been assumed to be $\mathcal{O}(1)$ in size. We also take $\beta_i = 1/2$ assuming symmetry in the anodic and cathodic current. For the small parameters, we take $\mathcal{D}_n = \mathcal{D}_p = \gamma = \nu_s = \nu_e = \mathcal{C}_n = 10^{-2}$. We also take $\mathcal{U}_p = \mathcal{U}_n = 2$, since $\log \mathcal{U}_i$ appears throughout and we wish to avoid $\log \mathcal{U}_i = 0$. We take $\mathcal{C}_p = 0.1$ in order to satisfy $\mathcal{C}_n \ll \mathcal{C}_p \ll 1$ and explicitly showcase the two capacitance subregimes. For symmetry, we consider $x_p = 0.34$ and $x_n = 0.67$ so that each domain takes up approximately a third of the battery cell, and we take $\theta = 0.5$ so that the effective charge is carried equally by lithium and the electrolytic salt. Since the porosity of electrodes is quite small, we take $\phi_e = \phi_{e,s} = 0.33$ and also assume that half of the volume is occupied by active material, i.e., $\phi_{a,i} = 0.5$. Due to our consideration of a discharge process, we will assume that the negative electrode is mostly saturated in lithium while the positive electrode is depleted and thus take $\xi_n = 0.9$ and $\xi_p = 0.05$. We will further assume that both electrodes have the same maximal concentration. Therefore, by definition of ξ_i and δ_i , the ratio $\xi_p/\xi_n = \delta_n/\delta_p$ must be held constant. As such, we fix $\delta_p = 1$, which restricts $\delta_n = 5.56 \times 10^{-2}$. These values are roughly based on those obtained using the dimensional parameter values in supplementary section SM3.

We simulate the full model, (2.4), (2.5), (2.7), using a second-order central difference discretization in space and backward Euler discretization in time, as detailed in supplementary section SM4. For all simulations, we take 50 interior cell-centers in each of the three domains and compute until the finite-time blow-up induced by (3.24). For the chosen parameters, this occurs at the nondimensional time $t = 297$ following (3.25), which corresponds to t_n .

We first compare the asymptotic and numerical profiles for the solid-phase lithium concentration. As predicted from the asymptotic analysis, the numerical profiles have weak spatial gradients. Therefore, we take spatial averages,

$$(4.1) \quad \langle c_{a,p} \rangle = \frac{1}{x_p} \int_0^{x_p} c_{a,p}(x, t) dx, \quad \langle c_{a,n} \rangle = \frac{1}{1 - x_n} \int_{x_n}^1 c_{a,n}(x, t) dx,$$

and plot them against the asymptotic expressions for the solid-phase concentration (3.17) in Figure 2. The agreement is excellent, with the numerical solution confirming the linear-in-time mean intercalation kinetics.

Numerical and asymptotic predictions of the steady-state concentration of lithium ions in the electrolyte are given in Figure 3. The simulation data is taken at the final

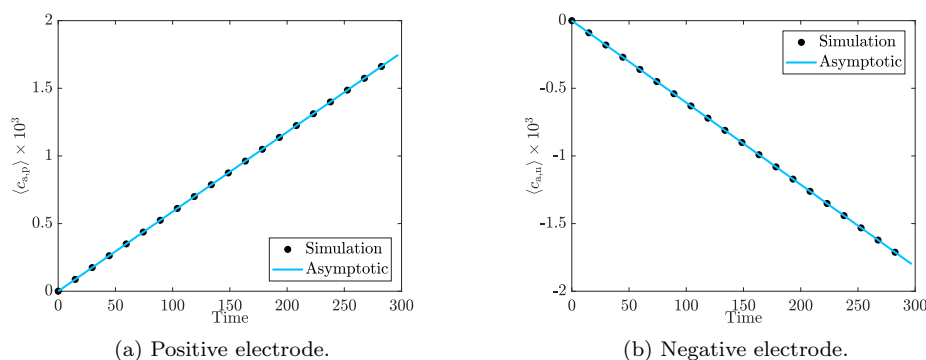


FIG. 2. Asymptotic solution (3.17) compared to the space-averaged simulated solid lithium concentration in each of the electrodes.

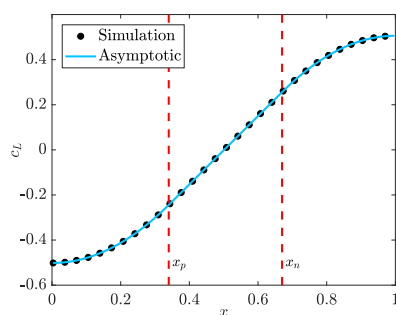


FIG. 3. Analytical steady state profile (3.18a) for the electrolyte concentration compared to numerical simulation at $t = 297$.

time $t = 297$. However, the steady-state profile is numerically achieved within a few time steps consistent with the $\mathcal{O}(1)$ time analysis. The asymptotic prediction is given by (3.18a).

We next plot the most relevant curve from an operational standpoint, the discharge curve. This is a plot of the cell potential (2.9) over the time span of discharge that captures the effects at all of the time regimes analyzed. The simulated data is compared to each of the asymptotic potentials (3.10), (3.13), (3.15), and (3.22) in Figure 4a. We also compare the simulated data to the composite reduced model (3.1) in Figure 4b.

For a given battery, the primary (dimensionless) parameter that can be varied is the C-rate, \mathcal{I} . Therefore, we demonstrate the robustness of the asymptotic reduction to this parameter in Figure 5 for high C-rates of 10 and 100, indicating fast discharge processes. We see that the quantitative agreement is excellent for the 10C case, but discrepancies occur at 100C. However, the qualitative agreement that is observed at 100C indicates the persistence of the regimes identified by the asymptotic analysis, suggesting there has been no change in the dominant physical mechanisms taking place during battery discharge.

The onset of discrepancies between the asymptotic and numerical solutions in Figure 5 can be understood by noticing that increasing \mathcal{I} is equivalent to increasing

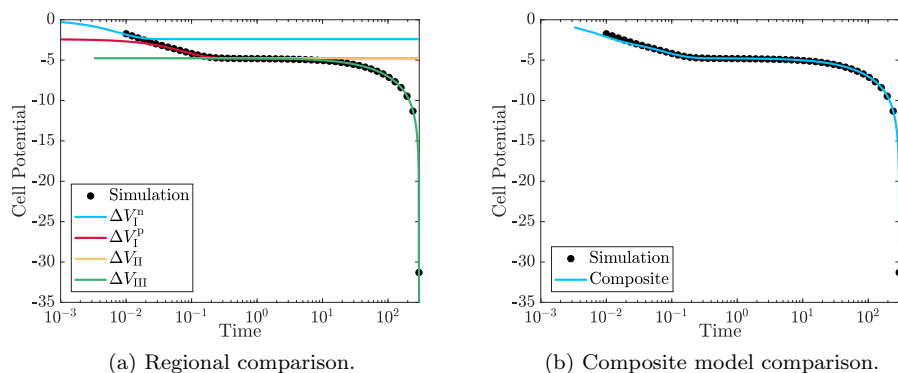


FIG. 4. Simulated discharge curve at 1C compared to the asymptotic cell potentials (3.10), (3.13), (3.15), and (3.22). The time axis is presented on a logarithmic scale to emphasize the asymptotic regions in time where each of the mechanisms discussed in subsections 3.2 to 3.4 dominate. The composite solution in panel (b) is obtained by solving (3.1).

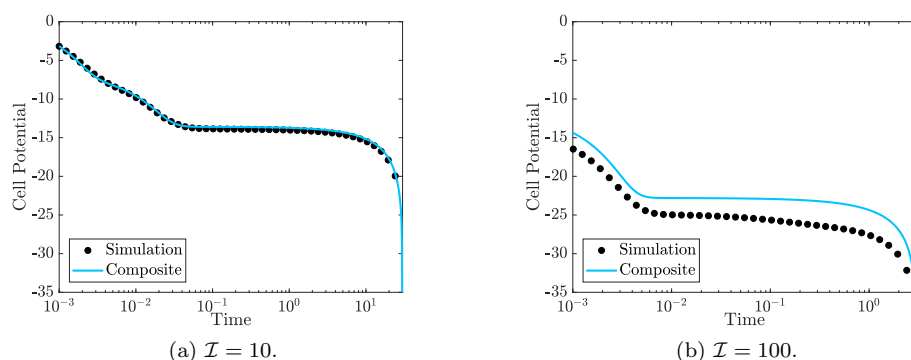


FIG. 5. Simulated discharge curves at 10C and 100C from numerical simulations of the full model (circles) and the composite reduced model (lines) given by (3.1).

the dimensional current i_0 , which impacts several of the nondimensional numbers. Thus, the failure of the asymptotic model around $\mathcal{I} = 100$ is unsurprising because it leads to ν_1 and γ becoming $\mathcal{O}(1)$ in magnitude. This has implications throughout the whole reduction which are based on (i) the concentration of electrolytic lithium $c_{L,i}$ not entering the leading-order Butler–Volmer kinetics and (ii) the electric potentials being spatially uniform. Simulations for $\mathcal{I} \leq 10$ show excellent agreement with the reduced model. Both high and low C-rate charges and discharges are important. Low C-rate discharges allow for accurate measurements of open-circuit voltages [42]. High C-rate charges are important for fast-charging mobile phones and electric vehicles. However, it is known that these high rates can lead to battery degradation and capacity fade. Therefore, further modelling and analysis in this regime is warranted [8].

4.1. Comparison with experimental data. We demonstrate the effectiveness of our reduced model by comparing it to discharge data from a real battery obtained by Li et al. [28]. The dimensional parameters are provided in Tables SM1 and SM2 of the supplementary material, and lead to $L/H = 2.0 \times 10^{-3}$, $\mathcal{D}_n = 1.5 \times 10^{-4}$,

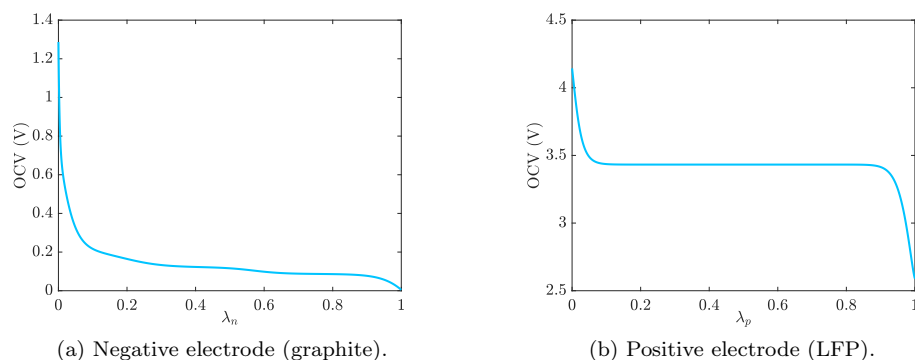
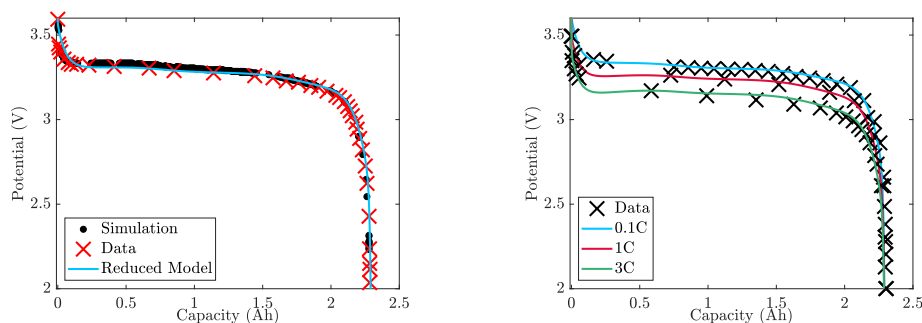


FIG. 6. Empirical open-circuit potentials used for a commercial lithium iron phosphate (LFP) battery from Li et al. [28].

$\mathcal{D}_p = 1.9 \times 10^{-4}$, $\mathcal{D}_A = 1.8$, $\gamma = 5.8 \times 10^{-2}$, $\nu_{a,n} = 6.8 \times 10^{-4}$, $\nu_{a,p} = 3.2 \times 10^{-2}$, $\nu_e = 2.1 \times 10^{-2}$, $\mathcal{G}_n = 4.9$, $\mathcal{G}_p = 5.3$, $\mathcal{C}_n = 7.4 \times 10^{-5}$, $\mathcal{C}_p = 5.1 \times 10^{-3}$, $\xi_n = 0.86$, $\xi_p = 0.02$, $\delta_p = 2.39$, and $\delta_n = 4.5 \times 10^{-2}$, which are of the presumed size for the asymptotic reduction in section 3. Therefore, the composite reduced model should sufficiently describe the battery being discharged. However, the theoretical open-circuit voltage (2.11) is not used by Li et al., who instead choose (dimensional) empirical formulae, $U_{\text{ref},i}$, as functions of state of charge for a commercial battery with electrodes made of LiFePO_4 and graphite. The open-circuit voltage curves are shown in Figure 6 with the corresponding empirical formula in section SM3 of the supplementary material. From our scaling, the state of charge, λ , can be related to the active solid lithium concentration via $\lambda_i = \xi_i(1 + \gamma\delta_i c_{a,i})$, and \mathcal{U}_i is determined by $(RT_a/F) \log \mathcal{U}_i = U_{\text{ref},i}(\xi_i)$.

The composite reduced model (3.1) is valid for all of the regimes, and we solve it numerically using the implicit solver `ode15s` in MATLAB until the state of charge of one of the electrodes decreases past zero or increases past one. This is equivalent to numerically finding the saturation/depletion times discussed in subsection 3.4. We compare our results to the data in Li et al. [28] for a 2C ($\mathcal{I} = 2$) discharge rate in Figure 7a, where excellent agreement is observed. An identical battery is used by Safari and Delacourt [43], who provide discharge data at various C-rates. We compare (3.1) to this data using the same parameters as before except with $\mathcal{C}_n = 2.69 \times 10^{-4}$, $\mathcal{C}_p = 5.4 \times 10^{-2}$, $\mathcal{G}_n = 1.33$, and $\mathcal{G}_p = 0.5$. These changes are due to Safari and Delacourt using different reaction rate constants for the kinetics compared to Li et al. The comparison between the reduced model and the data of Safari and Delacourt for discharge rates of 0.1C, 1C, and 3C is presented in Figure 7b. There is favorable agreement across all C-rates, with the accuracy of the model improving as the C-rate decreases. This demonstrates the feasibility of using the reduced model to predict discharge curves across a range of intermediate charging and discharging rates. The simulation results in each figure are rescaled dimensionally for appropriate comparison. Capacity is defined as the amount of charge used by the battery (in Ampere hours) and is scaled so that the time to full discharge corresponds to utilizing the entire charge of the battery. This is done to normalize the discharge process as different C-rates correspond to different discharge times.

It is important to point out that comparisons with experimental galvanostatic



(a) Comparison between a numerical simulation of the composite reduced model (3.1) (line), experimental battery discharge data at 2C (X) from Li et al. [28], as well as large-scale simulations of their P2D model (·).

(b) Comparison between a numerical simulation of the composite reduced model (3.1) at 0.1C (blue line), 1C (red line), and 3C (green line) with experimental battery discharge data (X) from Safari and Delacourt [43].

FIG. 7. Comparison between a numerical simulation of the composite reduced model (3.1) (line) and battery discharge data ('X'). Data in the left pane is a 2C discharge from Li and co-authors [28] as well as largescale simulations of their P2D model. Data in the right pane is from Safari and Delacourt [43] for 0.1C (blue), 1C (red), and 3C (green).

discharge curves only provide a means of assessing the validity of the reduced model in the third time regime. A more rigorous validation of the model would aim to probe the capacitance and diffusive regimes using experimental data from electrochemical impedance spectroscopy or sequential potentiostatic steps.

5. Discussion. The results in Figures 2–5 clearly demonstrate excellent agreement between the asymptotic theory and simulation. The asymptotic reduction is simple and elegant due mostly to the spatial independence of the electric potential owing to $\nu_i \ll 1$, which allows the problem to be decoupled. We are able to show that the solid-phase lithium concentration is always a linear function of time, reproducing the numerical results of Li et al. [28]. Using parameters from this paper we were also able to demonstrate strong agreement between our reduced model and actual battery discharge data in Figure 7a. To compare to the data, we numerically solved a pair of ordinary differential equations, which is in contrast to the model simulated by Li et al. [28] (also plotted in Figure 7a) which uses twelve highly nonlinear partial differential equations. While algorithmic efficiency and optimization can lead to fast solutions for a larger scale model of this type, a reduced model involving two simple differential equations requires much less sophistication to solve. Interestingly, the model solved by Li et al. uses the P2D approach discussed in section 2. Our reduced model also agrees favorably with their simulation results, validating that the volume-average approach used here is sufficient for matching discharge data under the presumed parameter size estimates. We demonstrate robustness of matching to discharge dynamics by also successfully comparing to data from Safari and Delacourt [43] at 0.1C, 1C, and 3C discharge rates in Figure 7b.

As a counterexample, our model is unable to predict the discharge curves measured by Srinivasan and Newman [48], which shows that the capacity of their LFP electrode strongly depends on the discharge rate. There is a nearly 90% reduction in capacity at a 5C discharge. Srinivasan and Newman compare their data to predictions from a “shrinking core” model, which accounts for phase separation by dividing each

solid particle into an Li-rich shell and an Li-depleted core. They demonstrate that at least two particle sizes are required to fit the data. This indicates that the discharge characteristics depend on the microscale dynamics, a feature that is unlikely to be captured by the volume-average approach used here.

An issue arises when comparing models to integrated data, such as the cell potential in Figure 7, which is that there is no spatial information to confirm or refute model predictions. For example, our volume-average approach predicts spatially homogeneous solid-phase concentration profiles in contrast to the P2D approach of Li et al. [28], yet both models produce results that agree with experimental data. Interestingly, the P2D model of Ranom [39, sect. 2.5.5] in the limit of fast diffusion in the electrode particles also predicts that particles (de)lithiate at the same rate. Srinivasan and Newman [48] could accurately predict their discharge curves using a shrinking core model. However, phase-field simulations and experiments have since shown that shrinking core models do not provide realistic descriptions of (de)lithiation [9, 30], and obtaining reasonable agreement requires parameter values that contradict those obtained through experimental measurement.

These differences in microscale modelling may not always be apparent when solely considering discharge dynamics, but may become more important for applications that aim to better understand the link between phase separation and battery behavior, stress development in particles, active material utilization, and degradation mechanisms. Recent experiments involving X-ray microscopy and nuclear magnetic resonance imaging of in situ lithium concentrations in a solid and electrolyte [29, 44, 27] may lead to more robust model predictions. Nevertheless, the results presented here demonstrate that a reduced model derived from volume averaging can be an effective tool for accurately predicting battery operation, one that offers substantial computational advantages over the P2D models commonly used in large-scale simulations [2, 3, 28, 43].

Contrasting desalination models [5, 6, 21, 31, 45], capacitive dynamics are seldom considered in LIB models. This is in spite of the fact that practical battery use may involve current pulses of short duration, where the battery response is dominated by capacitance effects [28, 35]. Incorporating capacitive dynamics into large-scale numerical solvers must be done with care, as sophisticated time-stepping schemes are required to correctly capture rapid changes that occur on the capacitive time scale, along with the normal operational changes that occur on larger time scales such as those associated with diffusion.

We have demonstrated that a volume-averaged model and its asymptotically reduced form are able to accurately predict battery behavior. Since the asymptotic solutions are determined from a system of two ordinary differential equations, they can vastly speed-up prototyping, as results can be quickly computed for a variety of parameters and compared to measured quantities. Battery designs that fail to fit the model may indicate the importance of modelling physics which are not presented here. Indeed, as battery material research advances, the electronic and mechanical properties of electrodes will need to be integrated into electrochemical models. For example, recent research [25, 49] has shown that the structure of nanowire-based electrodes can have an important impact on battery capacity and electrolyte interactions. As new physics are introduced into models, the computational times of large-scale simulations will rapidly increase. The use of simpler models obtained through a systematic reduction can make accurate computations more feasible, thereby accelerating the development of future battery technologies.

6. Conclusions. Overall, we have considered a simple electrochemical model for lithium-ion batteries. Using the fact that reaction kinetics dominate electrical effects ($\nu_i \ll 1$), we have shown that cell voltage behavior can be understood through a sequence of asymptotic regimes which elucidate simple underlying physical processes. These asymptotic regimes are likely to persist should features such as concentrated solution theory, concentration-dependent parameters, and separate liquid and solid geometries be incorporated into the model. The simplicity of the asymptotically reduced model will make it an appealing tool for battery scientists and engineers. Despite the emphasis on battery application, we have maintained generality so that a similar problem reduction may be amendable to other electrochemical systems with comparable features.

Acknowledgment. The first and fourth authors would like to thank the Centre de Recerca Matemàtica for hosting them during the completion of this manuscript.

REFERENCES

- [1] S. ABADA, G. MARLAIR, A. LECOCQ, M. PETIT, V. SAUVANT-MOYNOT, AND F. HUET, *Safety focused modeling of lithium-ion batteries: A review*, J. Power Sources, 306 (2016), pp. 178–192.
- [2] P. AMIRIBAVANDPOUR, W. SHEN, D. MU, AND A. KAPOOR, *An improved theoretical electrochemical-thermal modelling of lithium-ion battery packs in electric vehicles*, J. Power Sources, 284 (2015), pp. 328–338.
- [3] Z. AN, L. JIA, L. WEI, C. DANG, AND Q. PENG, *Investigation on lithium-ion battery electrochemical and thermal characteristic based on electrochemical-thermal coupled model*, Appl. Therm. Eng., 137 (2018), pp. 792–807.
- [4] J. BEAR, *Dynamics of Fluids in Porous Media*, Courier Corporation, New York, 1972.
- [5] P. BIESHEUVEL AND M. BAZANT, *Nonlinear dynamics of capacitive charging and desalination by porous electrodes*, Phys. Rev. E, 81 (2010), 031502.
- [6] P. BIESHEUVEL, Y. FU, AND M. Z. BAZANT, *Diffuse charge and faradaic reactions in porous electrodes*, Phys. Rev. E, 83 (2011), 061507.
- [7] J. CHAKRABORTY, C. P. PLEASE, A. GORIELY, AND S. J. CHAPMAN, *Combining mechanical and chemical effects in the deformation and failure of a cylindrical electrode particle in a Li-ion battery*, Int. J. Solids Struct., 54 (2015), pp. 66–81.
- [8] S. S. CHOI AND H. S. LIM, *Factors that affect cycle-life and possible degradation mechanisms of a Li-ion cell based on LiCoO₂*, J. Power Sources, 111 (2002), pp. 130–136.
- [9] D. A. COGSWELL AND M. Z. BAZANT, *Size-dependent phase morphologies in lifepo4 battery particles*, Electrochemistry Communications, 95 (2018), pp. 33–37.
- [10] S. DARGAVILLE AND T. W. FARRELL, *Predicting active material utilization in LiFePO₄ electrodes using a multiscale mathematical model*, J. Electrochem. Soc., 157 (2010), pp. A830–A840.
- [11] M. DOYLE, T. F. FULLER, AND J. NEWMAN, *Modeling of galvanostatic charge and discharge of the lithium/polymer/insertion cell*, J. Electrochem. Soc., 140 (1993), pp. 1526–1533.
- [12] M. DOYLE AND J. NEWMAN, *Analysis of capacity-rate data for lithium batteries using simplified models of the discharge process*, Journal of Applied Electrochemistry, 27 (1997), pp. 846–856.
- [13] T. W. FARRELL, C. P. PLEASE, D. McELWAIN, AND D. SWINKELS, *Primary alkaline battery cathodes a three-scale model*, J. Electrochem. Soc., 147 (2000), pp. 4034–4044.
- [14] T. R. FERGUSON AND M. Z. BAZANT, *Nonequilibrium thermodynamics of porous electrodes*, J. Electrochem. Soc., 159 (2012), pp. A1967–A1985.
- [15] T. R. FERGUSON AND M. Z. BAZANT, *Phase transformation dynamics in porous battery electrodes*, Electrochimica Acta, 146 (2014), pp. 89–97.
- [16] J. M. FOSTER, S. J. CHAPMAN, G. RICHARDSON, AND B. PROTAS, *A mathematical model for mechanically-induced deterioration of the binder in lithium-ion electrodes*, SIAM J. Appl. Math., 77 (2017), pp. 2172–2198, <https://doi.org/10.1137/16M1086595>.
- [17] A. C. FOWLER, *Mathematical Models in the Applied Sciences*, Cambridge Texts Appl. Math. 17, Cambridge University Press, 1997.
- [18] T. F. FULLER, M. DOYLE, AND J. NEWMAN, *Simulation and optimization of the dual lithium ion insertion cell*, J. Electrochem. Soc., 141 (1994), pp. 1–10.

- [19] P. M. GOMADAM, J. W. WEIDNER, R. A. DOUGAL, AND R. E. WHITE, *Mathematical modeling of lithium-ion and nickel battery systems*, J. Power Sources, 110 (2002), pp. 267–284.
- [20] A. GUDURU, P. W. NORTHROP, S. JAIN, A. C. CROTHERS, T. R. MARCHANT, AND V. R. SUBRAMANIAN, *Analytical solution for electrolyte concentration distribution in lithium-ion batteries*, J. Appl. Electrochem., 42 (2012), pp. 189–199.
- [21] F. HE, P. BIESHEUVEL, M. Z. BAZANT, AND T. A. HATTON, *Theory of water treatment by capacitive deionization with redox active porous electrodes*, Water Res., 132 (2018), pp. 282–291.
- [22] J. JOHANSEN, T. W. FARRELL, AND C. P. PLEASE, *Modelling of primary alkaline battery cathodes: A simplified model*, J. Power Sources, 156 (2006), pp. 645–654.
- [23] A. JOHNSON AND J. NEWMAN, *Desalting by means of porous carbon electrodes*, J. Electrochem. Soc., 118 (1971), pp. 510–517.
- [24] M. KAVIANY, *Principles of Heat Transfer in Porous Media*, Springer-Verlag, New York, 2012.
- [25] T. KENNEDY, M. BRANDON, F. LAFFIR, AND K. M. RYAN, *Understanding the influence of electrolyte additives on the electrochemical performance and morphology evolution of silicon nanowire based lithium-ion battery anodes*, J. Power Sources, 359 (2017), pp. 601–610.
- [26] T. KENNEDY, E. MULLANE, H. GEANEY, M. OSIAK, C. ODWYER, AND K. M. RYAN, *High-performance germanium nanowire-based lithium-ion battery anodes extending over 1000 cycles through in situ formation of a continuous porous network*, Nano Lett., 14 (2014), pp. 716–723.
- [27] S. A. KRACHKOVSKIY, J. M. FOSTER, J. D. BAZAK, B. J. BALCOM, AND G. R. GOWARD, *Operando mapping of li concentration profiles and phase transformations in graphite electrodes by magnetic resonance imaging and nuclear magnetic resonance spectroscopy*, J. Phys. Chem. C, 122 (2018), pp. 21784–21791.
- [28] J. LI, Y. CHENG, M. JIA, Y. TANG, Y. LIN, Z. ZHANG, AND Y. LIU, *An electrochemical-thermal model based on dynamic responses for lithium iron phosphate battery*, J. Power Sources, 255 (2014), pp. 130–143.
- [29] Y. LI, F. EL GABALY, T. R. FERGUSON, R. B. SMITH, N. C. BARTELT, J. D. SUGAR, K. R. FENTON, D. A. COGSWELL, A. D. KILCOYNE, T. TYLISZCZAK, M. Z. BAZANT, AND W. C. CHUEH, *Current-induced transition from particle-by-particle to concurrent intercalation in phase-separating battery electrodes*, Nat. Mater., 13 (2014), pp. 1149–1156.
- [30] J. LIM, Y. LI, D. H. ALSEM, H. SO, S. C. LEE, P. BAI, D. A. COGSWELL, X. LIU, N. JIN, Y.-S. YU, N. J. SALMON, D. A. SHAPIRO, M. Z. BAZANT, T. TYLISZCZAK, AND W. C. CHUEH, *Origin and hysteresis of lithium compositional spatiodynamics within battery primary particles*, Science, 353 (2016), pp. 566–571.
- [31] M. MIRZADEH, F. GIBOU, AND T. M. SQUIRES, *Enhanced charging kinetics of porous electrodes: Surface conduction as a short-circuit mechanism*, Phys. Rev. Lett., 113 (2014), 097701.
- [32] J. NEWMAN AND K. E. THOMAS-ALYEA, *Electrochemical Systems*, 3rd ed., John Wiley & Sons, Hoboken, NJ, 2004.
- [33] J. NEWMAN AND W. TIEDEMANN, *Porous-electrode theory with battery applications*, AIChE J., 21 (1975), pp. 25–41.
- [34] J. S. NEWMAN AND C. W. TOBIAS, *Theoretical analysis of current distribution in porous electrodes*, J. Electrochem. Soc., 109 (1962), pp. 1183–1191.
- [35] I. J. ONG AND J. NEWMAN, *Double-layer capacitance in a dual lithium ion insertion cell*, J. Electrochem. Soc., 146 (1999), pp. 4360–4365.
- [36] B. ORVANANOS, T. R. FERGUSON, H.-C. YU, M. Z. BAZANT, AND K. THORNTON, *Particle-level modeling of the charge-discharge behavior of nanoparticulate phase-separating li-ion battery electrodes*, J. Electrochem. Soc., 161 (2014), pp. A535–A546.
- [37] M. B. PINSON AND M. Z. BAZANT, *Theory of SEI formation in rechargeable batteries: capacity fade, accelerated aging and lifetime prediction*, J. Electrochem. Soc., 160 (2013), pp. A243–A250.
- [38] V. RAMADESIGAN, P. W. NORTHROP, S. DE, S. SANTHANAGOPALAN, R. D. BRAATZ, AND V. R. SUBRAMANIAN, *Modeling and simulation of lithium-ion batteries from a systems engineering perspective*, J. Electrochem. Soc., 159 (2012), pp. R31–R45.
- [39] R. RANOM, *Mathematical Modelling of Lithium Ion Batteries*, Ph.D. thesis, University of Southampton, Southampton, UK, 2014.
- [40] G. RICHARDSON, G. DENUAULT, AND C. P. PLEASE, *Multiscale modelling and analysis of lithium-ion battery charge and discharge*, J. Engrg. Math., 72 (2012), pp. 41–72.
- [41] G. RICHARDSON AND J. R. KING, *Time-dependent modelling and asymptotic analysis of electrochemical cells*, J. Engrg. Math., 59 (2007), pp. 239–275.

- [42] M. SAFARI AND C. DELACOURT, *Mathematical modeling of lithium iron phosphate electrode: galvanostatic charge/discharge and path dependence*, J. Electrochem. Soc., 158 (2011), pp. A63–A73.
- [43] M. SAFARI AND C. DELACOURT, *Modeling of a commercial graphite/LiFePO₄ cell*, J. Electrochem. Soc., 158 (2011), pp. A562–A571.
- [44] A. K. SETHURAJAN, S. A. KRACHKOVSKIY, I. C. HALALAY, G. R. GOWARD, AND B. PROTAS, *Accurate characterization of ion transport properties in binary symmetric electrolytes using in situ nmr imaging and inverse modeling*, J. Phys. Chem. B, 119 (2015), pp. 12238–12248.
- [45] K. SINGH, H. BOUWMEESTER, L. DE SMET, M. BAZANT, AND P. BIESHEUVEL, *Theory of water desalination with intercalation materials*, Phys. Rev. Appl., 9 (2018), 064036.
- [46] R. B. SMITH AND M. Z. BAZANT, *Multiphase porous electrode theory*, J. Electrochem. Soc., 164 (2017), pp. E3291–E3310.
- [47] R. B. SMITH, E. KHOO, AND M. Z. BAZANT, *Intercalation kinetics in multiphase-layered materials*, J. Phys. Chem. C, 121 (2017), pp. 12505–12523.
- [48] V. SRINIVASAN AND J. NEWMAN, *Discharge model for the lithium iron-phosphate electrode*, J. Electrochem. Soc., 151 (2004), pp. A1517–A1529.
- [49] K. STOKES, H. GEANEY, G. FLYNN, M. SHEEHAN, T. KENNEDY, AND K. M. RYAN, *Direct synthesis of alloyed Si_{1-x}Ge_x nanowires for performance-tunable lithium ion battery anodes*, ACS Nano, 11 (2017), pp. 10088–10096.
- [50] J.-M. TARASCON AND M. ARMAND, *Issues and challenges facing rechargeable lithium batteries*, Nature, 414 (2001), pp. 359–367.
- [51] K. E. THOMAS-ALYEA, C. JUNG, R. B. SMITH, AND M. Z. BAZANT, *In situ observation and mathematical modeling of lithium distribution within graphite*, J. Electrochem. Soc., 164 (2017), pp. E3063–E3072.
- [52] L. O. VALØEN AND J. N. REIMERS, *Transport properties of LiPF₆-based Li-ion battery electrolytes*, J. Electrochem. Soc., 152 (2005), pp. A882–A891.
- [53] Q. WANG, P. PING, X. ZHAO, G. CHU, J. SUN, AND C. CHEN, *Thermal runaway caused fire and explosion of lithium ion battery*, J. Power Sources, 208 (2012), pp. 210–224.
- [54] S. WHITAKER, *Advances in theory of fluid motion in porous media*, Ind. Eng. Chem., 61 (1969), pp. 14–28.
- [55] R. ZHAO, J. LIU, AND J. GU, *Simulation and experimental study on lithium ion battery short circuit*, Applied Energy, 173 (2016), pp. 29–39.